Designing Optimal Bandwidth Synthesis Arrays for VLBI

P. W. Gorham[1]

An approach toward choosing optimal sets of frequency channels for bandwidth synthesis in radio interferometry is presented and applied to 14-channel 2.2-/8.4-GHz (S-/X-band) very long baseline interferometry (VLBI) observations. It is shown that arrays with nonredundant autocorrelations in general have a higher ratio of the delay resolution function central maximum to the nearby side lobes than do arrays with partially or fully redundant channel spacings.

Results from an algorithm that selects such arrays are presented, and delay resolution functions for a variety of channel sequences are documented. A proposed near-optimal sequence for mode-A S-/X-band VLBI observations (which use both upper and lower side bands as compared with the single-side-band mode-C observations) is presented and shown to give significantly improved side-lobe behavior as compared with a commonly used mode-C sequence adapted to mode A.

I. Introduction

The measurement precision of group delay achieved in very long baseline interferometry (VLBI) observations depends strongly on the bandwidth of the observation. Thus, the widest possible bandpass should be used. However, because of limitations in recording rate, it usually is necessary to synthesize a large effective bandwidth from a set of much narrower frequency channels that are spread out across the band. This technique is called bandwidth synthesis (BWS) and was first described in detail for VLBI observations by Rogers [8].

In simplified terms, the relative delay between two antennas on an interferometer baseline is determined by sampling the delay resolution function (DRF) of the two antenna signals as a function of time delay until the central maximum is found above the noise. The delay precision will depend upon the width of this delay function's central maximum, and the confidence level of the detection of the maximum will depend upon the degree to which the highest side lobe, or secondary maximum of the delay function, is confused with the central peak. This in turn depends on the signal-to-noise ratio (SNR) of the observations.

Thus, the problem of optimizing the BWS array centers on getting the highest resolution with the minimum side lobes. Actually, side lobes that are large, but far enough from the central maximum that they can be rejected by other considerations (such as a priori knowledge of the delay), may be allowed. It is only those side lobes that may be confused with the central maximum that are problematic.

[1] Tracking Systems and Applications Section.

In what follows, we describe the delay function and its relation to the autocorrelation of the bandwidth synthesis channel array. This will provide an analytical framework to understand further the role that redundant channel spacings play in influencing the characteristics of the delay function. After arguing that nonredundant arrays are to be preferred for bandwidth synthesis, we show results of an algorithm to construct such arrays and compare the arrays with other results. We conclude with an Appendix summarizing analysis of some arrays recently used in geodetic VLBI observations by JPL and Goddard Space Flight Center (GSFC).

II. Delay Function

This section will present analysis of the delay function in terms of the autocorrelation of the frequency channel array. The purpose will be to argue that nonredundant filter-bank channel spacings are optimal for achieving the best global signal-to-noise ratio in the amplitude of the DRF. Since the analysis is somewhat detailed, readers who are willing to accept the premise that nonredundant configurations are preferable may wish to skip to the next section, which describes the algorithm that was implemented.

The DRF $\gamma(\tau)$ is the Fourier transform of the spectral bandpass response (cf., [3]). Thus,

$$\gamma(\tau) = \int_0^F G(\nu) e^{-2\pi i \nu \tau} d\nu \tag{1}$$

where F is the upper frequency limit and $G(\nu)$ is the normalized spectral density for frequency ν, which is zero for $\nu > F$. Here we have assumed that $G(\nu)$ is nonzero only for $\nu \geq 0$.

For an array of N square-bandpass filters centered at frequencies ν_j,

$$G(\nu) = b(\nu) \otimes \sum_{j=1}^{N} \delta(\nu - \nu_j) \tag{2}$$

where $\delta(\nu)$ is the Dirac delta function, $\otimes$ indicates convolution, and $b(\nu)$ provides the shape of the single channel bandpass, which, for a square bandpass of width Δf, implies

$$b(\nu) = 1, \ \nu \leq \pm\frac{\Delta f}{2}, \quad b(\nu) = 0 \text{ otherwise} \tag{3}$$

Making use of Eq. (1), and applying the Fourier convolution theorem, we find

$$\gamma(\tau) \ = \ |\sin c(\Delta f \tau)| \times \sum_{j=1}^{N} e^{-2\pi i \nu_j \tau} \tag{4}$$

where the $\sin c$ function is defined as

$$\sin c(x) \equiv \frac{\sin(\pi x)}{\pi x} \tag{5}$$

Equation (4) shows that the delay function is a sum of complex phasors, with an overall envelope modulated by Fourier transform of the individual filter channel bandpass shape.

A. Autocorrelation of $G(\nu)$

Although the phase of $\gamma(\tau)$ may be of interest for determining the effects of channel phase errors, we consider only the amplitude here. Equation (4) may be used to determine $|\gamma(\tau)|$ directly; however, it is instructive to estimate $|\gamma(\tau)|$ by determining first the autocorrelation function (ACF) $A(f)$ of $G(\nu)$. The amplitude spectrum can be determined from $A(f)$, since the square of the amplitude spectrum and the ACF are related as a Fourier transform pair. Thus,

$$|\gamma(\tau)|^2 = \int_{-F}^{F} A(f) e^{-2\pi i f \tau} df \tag{6}$$

where f is the frequency lag in the ACF $A(f)$. The integration limits have now been extended to both positive and negative values of the frequency lag f since $A(f)$ is symmetric in f by definition:

$$A(f) = \int_{0}^{F} G(\nu) G^*(\nu - f) d\nu \tag{7}$$

and

$$A(-f) = A(f) \tag{8}$$

Substituting Eq. (2) into Eq. (7), we find

$$A(f) = \Lambda(\Delta f) \otimes \sum_{i=1}^{N} \sum_{j=1}^{N} \delta(\nu_i - \nu_j - f) \tag{9}$$

where $\Lambda(\Delta f)$ is the ACF of the bandpass function $b(\nu)$, which is triangular with base width $2\Delta f$ for a square bandpass of width Δf.

Equation (9) shows that the ACF depends on the intervals $\nu_i - \nu_j$ between filter-bank channels rather than on the absolute value of the channel frequency. The functional form of $A(f)$ can be determined by inspection. At $f = 0$, the ACF value will equal the number of channels (assuming $b(\nu)$ is normalized to unit amplitude) since they will all self-correlate. At any other frequency lag f, the magnitude of $A(f)$ will depend on how many pairs of channels satisfy $\nu_i - \nu_j = f$.

There are three cases here to consider: (1) the case when all channel spacings are equal, or the case of complete redundancy; (2) the nonredundant case; and (3) the intermediate case of partial redundancy.

B. Complete Redundancy

In the completely redundant case, we have a uniform interval between adjacent frequency channels, e.g.,

$$\nu_i - \nu_{i-1} = \frac{F}{N-1} \tag{10}$$

where F is the total bandwidth over which the channels are spread and N is the number of channels. The entire set of differences will be characterized by

$$\nu_i - \nu_j = \frac{kF}{N-1}, \quad k = 0, \cdots, N-1 \tag{11}$$

which means that all intervals will be multiples of the basic interval.

For this case, Eq. (9) gives

$$A(f) = \Lambda(\Delta f) \otimes \left[N\delta(f) + \sum_{k=1}^{N-1} (N-k) \left(\delta(\frac{kF}{N-1} - f) + \delta(\frac{kF}{N-1} + f) \right) \right] \tag{12}$$

In this case, $A(f)$ consists of a single central maximum at $f = 0$ with amplitude N and a symmetric series of secondary peaks spaced at intervals of $F/(N-1)$, and amplitude that falls off linearly at larger frequency intervals.

An example of this for 9 channels distributed evenly over a range of 73 possible frequency values is shown in Fig. 1. Here the ACF is shown without the individual channel bandpass convolution; thus, each entry in the plot indicates the number of times that interval occurs in the channel array.

Using Eq. (6) for the completely redundant case, evaluating the Fourier transform, and using Euler's relation, we have

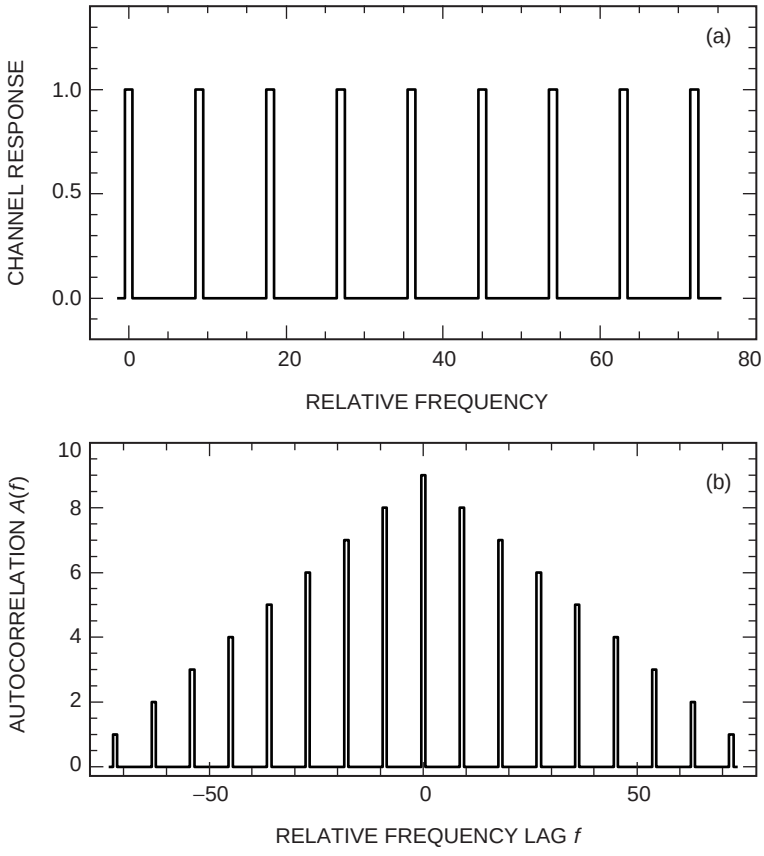

Fig. 1. The channel array for (a) the even spacing case and (b) the corresponding autocorrelation function.

$$|\gamma(\tau)|^2 = \sin c^2(\Delta f \tau) \left[N \; + \; 2 \sum_{k=1}^{N-1} (N-k) \cos\left(2\pi \frac{kF}{N-1} \tau \right) \right] \tag{13}$$

where $\sin c^2(\Delta f \tau)$ is the Fourier transform of the triangular channel ACF $\Lambda(\Delta f)$ (cf., [3]), which provides a modulated envelope to $|\gamma(\tau)|^2$. Thus, $|\gamma(\tau)|^2$ here consists of a sum of fringes, all with integer multiples of one basic frequency, plus a constant term proportional to N, which arises from the $k = 0$ terms.

The central maximum of this function has an amplitude

$$|\gamma(0)|^2 = N^2 \tag{14}$$

Since all of the fringes represented by this equation will have local maxima at integer multiples of $\tau = (N-1)/Fk$, they will constructively interfere in the amplitude spectrum, with a central maximum of this amplitude at $\tau_0 = 0$ and secondary maxima at intervals of

$$\tau_m = \frac{m(N-1)}{F}, \; m = 1, 2, \cdots \tag{15}$$

which will occur with an amplitude

$$|\gamma(\tau_m)| = N \sin c \left(\Delta f \frac{m(N-1)}{F} \right) \tag{16}$$

Since the phase angles in the cosine terms are all multiples of 2π, the amplitude of these side lobes is equal to that of the central lobe apart from the effect of the envelope of the individual channel bandpass function. The first null of this envelope occurs at

$$\tau = \frac{1}{\Delta f} \tag{17}$$

Since the total bandpass F typically is much larger than the individual channel bandpass Δf, the envelope of the $|\sin c|$ modulation will only slowly reduce the amplitude of the side lobes for this completely redundant case.

For example, if $F = 370$ MHz, $\Delta f = 4$ MHz, and $N = 9$ channels, the first large side lobe near the central maximum will occur at a delay of

$$\tau_1 = \; \frac{8}{370 \times 10^6} \sim 22 \text{ ns} \tag{18}$$

at an amplitude relative to the central maximum of

$$\frac{\sin(\pi(4 \times 10^6)\tau_1)}{\pi(4 \times 10^6)\tau_1} = 0.99 \tag{19}$$

which shows that evenly spaced channels produce a delay function in which nearby side lobes are very easily confused with the central maximum for typical values of the frequency parameters.

Figure 2 shows an example of this effect, with a delay function calculated for 8210 to 8575 MHz (X-band), using 9 equally spaced filter channels of 4-MHz bandpass. (Here the individual channel bandpass function actually was an 8-pole Butterworth filter rather than a rectangular shape, so the secondary maxima do not follow Eq. (19) exactly.) Figure 2(a) shows the overall envelope of modulation in the delay function, due to the channel bandwidth, and Fig. 2(b) shows the region near the central maximum. Clearly the usefulness of this type of array is low due to the problem of side-lobe confusion.

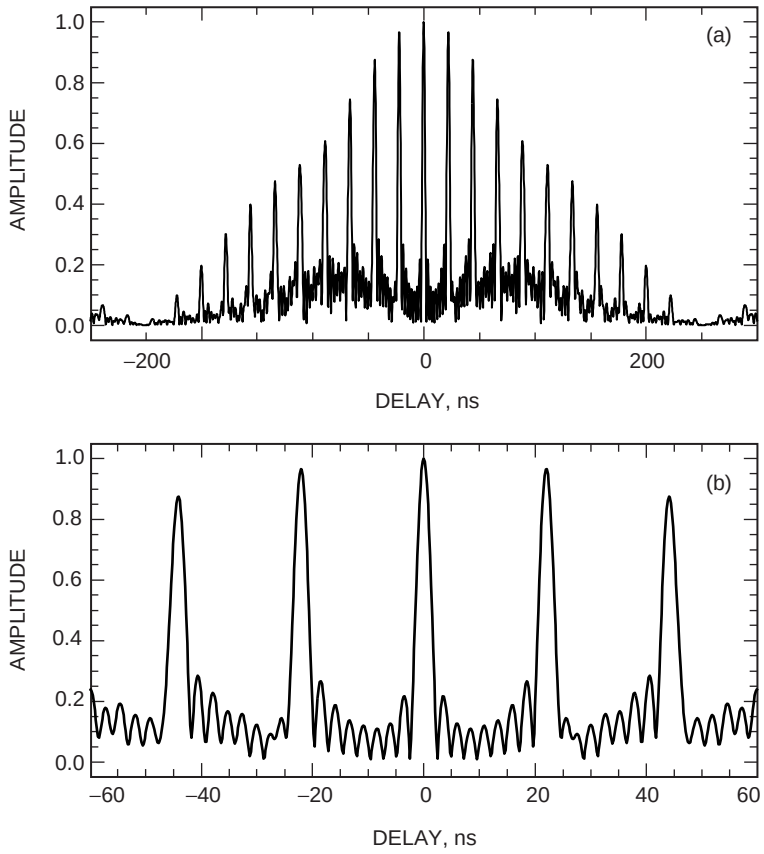

Fig. 2. The delay spectrum for (a) a filter channel array with even spacing across the band (i.e., a completely redundant autocorrelation) and the resulting side-lobe series in the delay amplitude spectrum and (b) a different magnification on the same spectrum. The assumed total bandpass was 370 MHz, and the individual channels were 4-MHz wide. The effects of the global sin *c* modulation are also evident in Fig. 2(a), with its first null at $\pm$(4 MHz)$^{-1}$ = $\pm$250 ns.

C. The Nonredundant and Partially Redundant Cases

In the nonredundant case, all of the spacings between individual spectral channels are unique, e.g., $\nu_i - \nu_j = f$ is only satisfied for one pair of channels (i, j) for each f. The ACF thus consists of a central peak and $N(N-1)$ secondary peaks of unit amplitude, half of which are the mirror images of the other half. Thus, there are

$$M = \frac{N(N-1)}{2} \tag{20}$$

independent spacings. For this ACF, the square of the delay function from Eqs. (6) and (9) is

$$|\gamma(\tau)|^2 = \sin c^2(\Delta f \tau) \int_{-F}^{F} \sum_{i=1}^{N} \sum_{j=1}^{N} \delta(\nu_i - \nu_j - f) e^{-2\pi i f \tau} df \tag{21}$$

The integral over the delta functions yields a term at each point where $\pm f = \nu_i - \nu_j$. Thus,

$$|\gamma(\tau)|^2 = \sin c^2(\Delta f \tau) \sum_{i=1}^{N} \sum_{j=i}^{N} \left[e^{-2\pi i(\nu_i - \nu_j)\tau} + e^{2\pi i(\nu_i - \nu_j)\tau} \right] \tag{22}$$

which can be written (using Euler's equation) as a sum of cosine fringes:

$$|\gamma(\tau)|^2 = \sin c^2(\Delta f \tau) \left[N + 2 \sum_{i=1}^{N-1} \sum_{j>i}^{N} \cos(2\pi(\nu_i - \nu_j)\tau) \right] \tag{23}$$

The constant background term N comes from the self-correlation of each channel. The amplitude of the central maximum again is

$$|\gamma(0)|^2 = N^2 \tag{24}$$

as expected.

The important physical aspect of Eq. (23) is that it represents a sum of phasors, each of which has unit amplitude and whose frequency is determined by the channel spacing $\nu_i - \nu_j$. If all of the spacings are unique, then we are in the nonredundant regime; if any of the spacings are repeated, we are in the partially redundant regime.

1. Peak-to-Side-Lobe Ratios for Nonredundant and Partially Redundant Arrays. In Appendix A, we present analysis that gives an analytical estimate of the rms side-lobe value of $|\gamma(\tau)|^2$ with respect to the central maximum. The results are stated here:

$$\sigma^2(|\gamma|^2; K) = N^2 - N + 4K \tag{25}$$

where $\sigma^2(|\gamma|^2; K)$ is the variance of the side lobes and the factor K expresses the level of redundancy as the number of pairs of channels that have equal spacings (to within the resolution of the individual channel width Δf).

The peak-to-rms-side-lobe ratio (PSR) for the power spectrum then can be expressed as

$$PSR(N, K) = \frac{|\gamma(0)|^2 - \langle |\gamma(\tau)|^2 \rangle}{\sqrt{N^2 - N + 4K}}$$

$$= \frac{N^2 - N}{\sqrt{N^2 - N + 4K}} \tag{26}$$

For the nonredundant case ($K = 0$), this reduces to

$$PSR(N,0) = \sqrt{N^2 - N} \tag{27}$$

It is evident from these results that the nonredundant case always will have the highest PSR in general, and that the difference for moderate N can be significant, even for low levels of redundancy.

For detection of the central maximum at a high confidence level, the relevant quantity is not necessarily the rms side-lobe level, but rather the maximum side lobe that may be confused with the central peak. For low-to-moderate levels of redundancy, the resulting distribution of side lobes is known once the mean and rms are known, since the variance is approximately equal to the mean. This corresponds to the well-known case of a power spectrum of impulsive or Poisson events, as mentioned above. For this case, the distribution function of side-lobe peak values is given by

$$P(Z \geq \mu) \propto \exp\left(\frac{-Z}{\mu}\right) \tag{28}$$

where Z is the measured peak value of a given side lobe that exceeds the mean power spectrum value (or variance) μ. This result strictly applies only to a stationary Poisson process but indicates that the behavior of the maximum side lobe in a DRF will tend to correlate to the rms side-lobe level. Although this does not prove that nonredundant arrays will yield *maximum* side lobes that are always *lower* than those of any given partially redundant array, it suggests that restricting the choice to nonredundant arrays generally will yield improved peak-to-side-lobe results.

Figure 3 plots an example of the behavior of the PSR as a function of increasing redundancy for a 9-channel array, for which there are 36 possible independent spacings. From the plot, it is evident that the loss in PSR is steepest at low levels of partial redundancy.

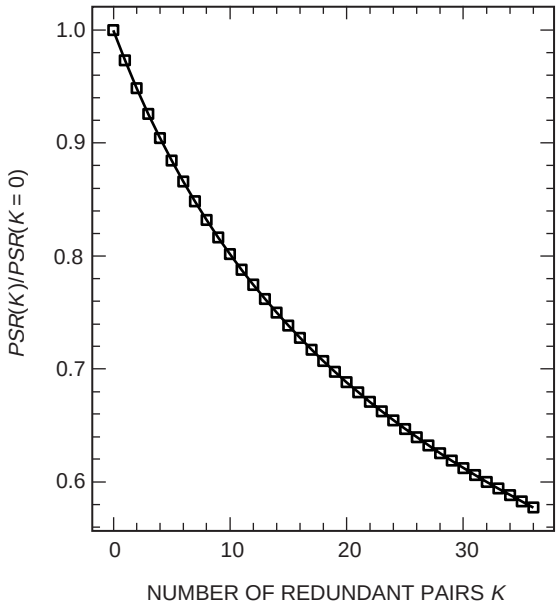

Fig. 3. The normalized PSR in the DRF spectrum plotted as a function of the redundancy parameter, *K*, which counts the number of repeated channel pair spacings (a nine-channel array assumed).

2. Other Considerations: Delay Resolution. Given that the highest PSR in general will be achieved for nonredundant configurations of channel spacings in a frequency channel array, there is one other significant consideration in choosing among such arrays: the delay resolution, or precision with which the delay can be measured once the central maximum of the delay resolution function has been found. This precision is determined mainly by the width of the central maximum of the DRF, and this width is a function of the particular configuration of the channel spacings and of the individual channel width.

This article has focused primarily on achieving the best peak-to-side-lobe ratio in the DRF, but given two nonredundant configurations with equal PSRs, the choice of configurations also must consider delay precision, and the present analysis does not provide any insight into which nonredundant arrays will have the best delay precision. In fact, under some circumstances, partial redundancy may be tolerable if the loss in PSR is offset by an improvement in the delay precision. However, we do not attempt to analyze such conditions here, since it requires a detailed consideration of the SNR of the observations that go into producing the DRF as well as the PSR of the DRF itself.

A later section will describe an empirical method by which the width of the central peak of the DRF was included in the choice of channel configurations, but an analytical framework for this is beyond the scope of this article.

D. Example of a Nonredundant ACF and Its Delay Function

Figure 4(a) shows an example of a nonredundant set of frequency channels, again at X-band with 9 channels. The positive half of the ACF appears in Fig. 4(b), and the delay function for this is shown in Fig. 5. Figure 5(a) gives a broad view of the delay amplitude spectrum, and Fig. 5(b) zooms in to the neighborhood of the central maximum. Here we also have plotted, in dashed lines, the spectrum from the completely redundant case (cf., Fig. 2) to show the difference near the central maximum. In the immediate neighborhood of the peak, the completely redundant case gives much lower side lobes, but the proximity of the large peaks in the redundant DRF produces a much reduced global PSR compared with the redundant case. It also is worth noting that the delay precision of the nonredundant configuration is about 30 percent better than that of the redundant case at the half maximum point.

III. Generating Nonredundant Arrays

Nonredundant configurations are of interest in other areas of interferometry, particularly aperture synthesis. Golay has provided a tree-search algorithm for generating two-dimensional nonredundant arrays that could be adapted to a one-dimensional case [4]. Moffet presents some aperture synthesis arrays with low levels of redundancy that are of interest as partially redundant cases [7]. Recently, Kopilovich and Sodin presented analysis of aperiodic antenna arrays for interferometry that utilize nonredundant spacing of elements [6]. We have as yet found no comparable treatment of nonredundant arrays for bandwidth synthesis in the literature, so the techniques proposed for the aperture synthesis cases represent the only experience that we can draw on at present.

Methods exist for generating nonredundant configurations through the use of cyclic difference sets [1]; such techniques have been used in two dimensions to produce arrays for coded-aperture imaging [2,5]. In general, these methods are adaptable to generating bandwidth synthesis arrays when there are no other constraints on channel spacings other than the nonredundancy requirement. However, it has not yet been proven that cyclic difference set generators produce complete groups of such arrays. In the present case, there are a number of practical constraints that led to adopting a more empirical approach

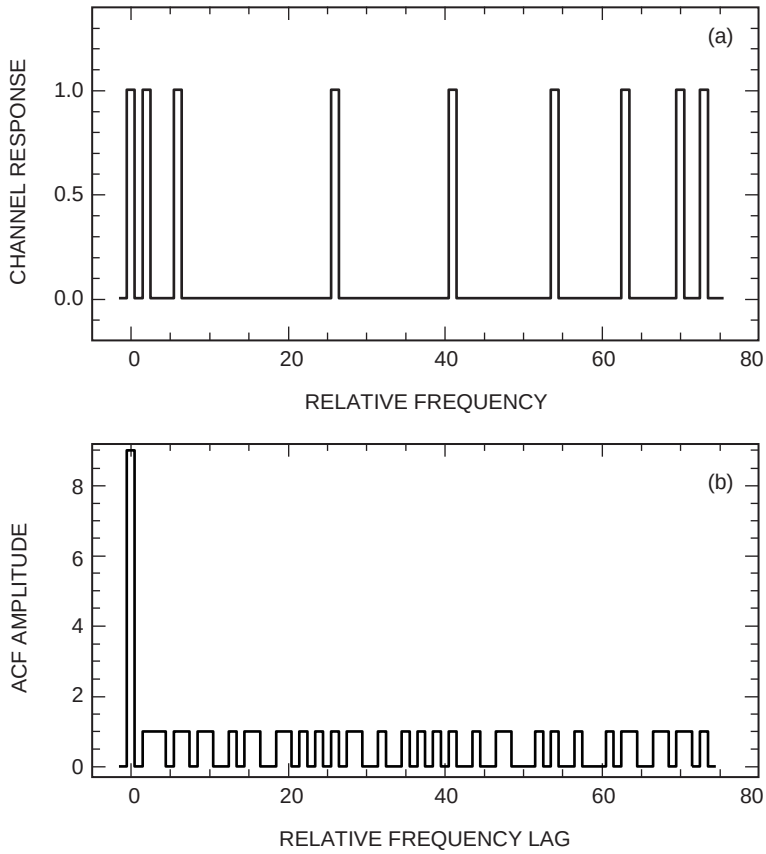

Fig. 4. An array example: (a) a nonredundant set of channels generated for X-band with 9 channels, 4-MHz wide, spanning a 370-MHz total synthesized band and (b) the positive side of the autocorrelation of this array, with the single-channel convolution removed for clarity. Thus, each bin in the ACF corresponds to a single interval between channels in Fig. 4(a), and it is evident that there are no overlapping intervals.

to generation of the BWS arrays. For example, there are constraints that come from electronic noise in the video downconverters, such as a requirement that the individual channel bandpass avoid multiples of 5 MHz and other troublesome resonance frequencies within the system. For these reasons, we have chosen simply to select the nonredundant arrays from numerically generated random patterns. These are initially sifted by inspection of their ACFs for redundancy and application of the additional frequency–noise constraints. This approach is inefficient but straightforward, using a computer, and allows many thousands of possible arrays to be inspected for optimal characteristics, including arrays that might not be generated using analytical approaches, if the set of such arrays is found to be mathematically incomplete.

A similar approach was used by Rogers [8] but without the additional constraint of nonredundancy, which significantly narrows the search. As Moffet has noted, this trial-and-error approach is feasible at present only for $N \leq 10$, since the number of possible configurations grows factorially, and for $N = 9$, $M \sim \epsilon 10^9$ where $\epsilon \leq 10^{-2}$ is the ratio of the number of nonredundant configurations to the total, which is a strong function of N [7]. To generate optimal arrays with much larger numbers will require a refinement of the algorithm, perhaps through use of generators of cyclic difference sets as noted above.

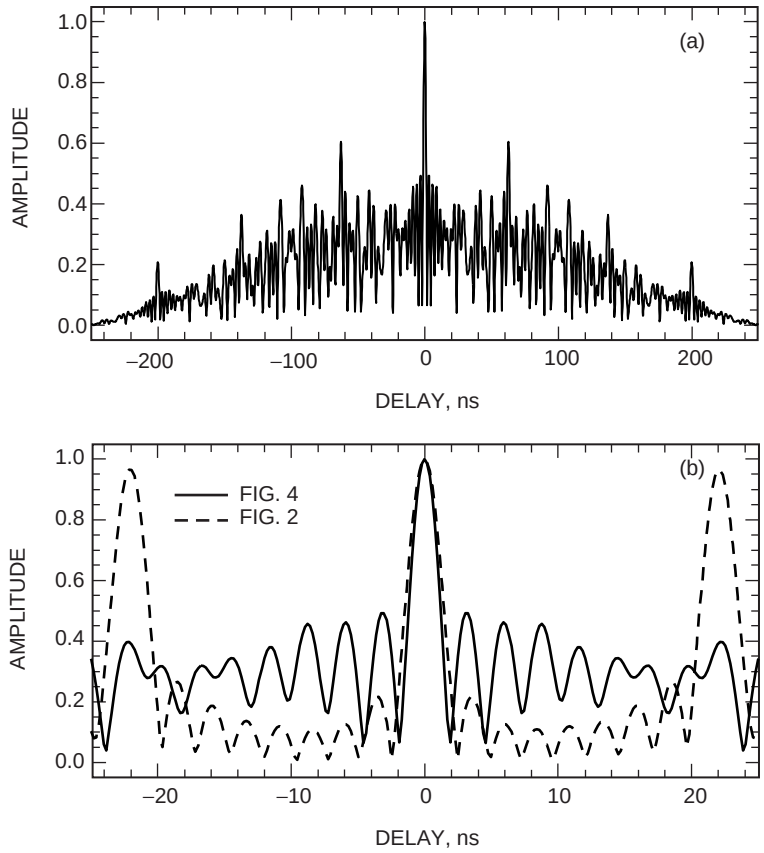

Fig. 5. The delay spectrum of the filter-bank array shown in Fig. 4, at two magnifications: (a) a broad view and (b) a zoom in to the neighborhood of the central maximum.

A. Algorithm

Our approach to finding and characterizing optimal filter-bank arrays was as follows:

(1) Generate a frequency channel pattern by randomly distributing the channels across the aperture. Two channels are initially fixed at the edges of the band to ensure high central-lobe resolution; this fixes the maximum bandwidth, F, that is synthesized.

(2) Calculate all intervals between channels to determine the ACF. Reject any array pattern that has redundant spacings. Reject any patterns that do not satisfy the constraints on frequency multiples as noted above.

(3) Estimate the delay spectrum for the nonredundant array pattern using a discrete Fourier transform over a suitable window (cf., within the initial few lobes of the envelope of the channel bandpass $\sin c$ function) near the central maximum. Normalize the spectrum to the central maximum.

(4) Determine the highest side lobe, S_{max}, in the window.

(5) Determine the full width at half maximum (FWHM), W, of the central lobe to estimate the delay resolution.

(6) Form a figure of merit, Φ, which is defined as

$$\Phi = S_{max} \times W^z \tag{29}$$

where z is chosen to weight the resolution requirement to the desired degree over the minimum side-lobe requirement.

(7) The sequence above is repeated for a large number of trials, and the array with the smallest value of Φ is selected.

B. Testing

The code that performed the spectrum estimation was checked by reproducing Rogers' spectrum for a 6-channel array that he recommended for bandwidth synthesis over a 7.47-MHz bandpass with 60-kHz channels [8]. Then, to ensure that the algorithm could find comparable or improved arrays, these parameters were used in the search algorithm, and an array was chosen after 1000 trials (requiring about 2 min on a Sparc Ultra-2), using a FWHM weighting of $z = 0.5$, with somewhat improved characteristics over Rogers' array. The array generated is the sequence (0, 9, 14, 71, 101, 123) $\times$ 60 kHz, which may be compared to Rogers' original array of (0, 1, 3, 7, 15, 31) $\times$240 KHz.

A comparison of the spectra appears in Fig. 6. Figure 6(a) shows the same range as shown in [8], with Rogers' delay function in dashed lines. The side lobes are comparable in both spectra. Figure 6(b) shows

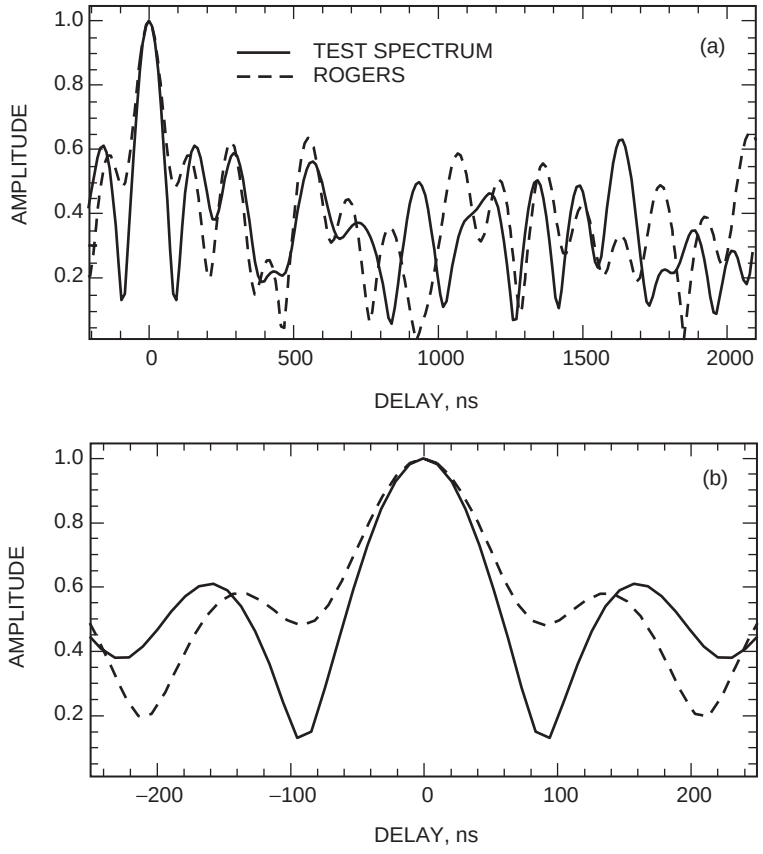

Fig. 6. The delay function for a test spectrum (a) generated according to the parameters used by Rogers [8] and (b) the region near the central maximum.

the region near the central maximum, where the array function generated in the present work can be seen to have approximately 15 percent better delay resolution, measured at 80 percent of the maximum. This is due primarily to the resolution weight provided by the figure of merit in the algorithm. Rogers' approach did not emphasize delay resolution as compared with side-lobe performance.

IV. Results

One of the goals of this effort was to produce an algorithm for generating BWS arrays for the 14-channel system for VLBI observations, using both the upper and lower side bands (this is known as a mode-A observation), which increases the channel bandwidth from 2 to 4 MHz. This improves the *measurement* SNR significantly. However, the increase from 2 to 4 MHz in channel bandwidth introduces problems for existing arrays, because the issues of channel spacing redundancy become more critical for wider channels, as also do the related issues of avoiding resonance frequencies and similar concerns. Thus, simply using channel arrays designed for 2-MHz channels without consideration of DRF PSR resulting from the channel array likely will lead to suboptimal improvement in the final result.

For the following, we have assumed that nine channels are used in X-band (8.4 GHz) and five in S-band (2.2 GHz). The bandwidth at X-band is restricted to $\Delta F = 370$ MHz because of edge effects on the band. Channels are 4-MHz wide but are spaced in 5-MHz windows to avoid interference with local oscillators, and the center frequencies are offset slightly to give the best arrangement of calibration tones within the 0.5-MHz subbands of each channel.

In Appendix B, we document the delay resolution functions (DRFs) for some existing BWS arrays in recent use in 14-channel VLBI at S-/X-band. Appendix B also looks at the issue of channel dropouts and the effect they have on the DRF.

A. X-band (8.2 to 8.6 GHz)

We present here one example of a near-optimal array generated for X-band. The array has a DRF with improved side lobes as compared with a reference delay function obtained from a BWS array used for 1990 VLBI observations at 2 MHz. Many other comparable arrays can be obtained for various forms of the figure of merit Φ above, but this one is representative of the best of them. Improved delay precision also can be obtained, but never (for the X-band constraints imposed) more than about 5 percent in the runs performed to date, and at the expense of a typically 50 percent higher side-lobe amplitude.

Figures 7(a) and 7(b) show the array pattern and ACF obtained from the sequence:

$$f_i = (8212 + \nu_i \times 5) \text{ MHz} \tag{30}$$

$$\nu_i = (0, 2, 6, 26, 41, 54, 63, 70, 73) \tag{31}$$

which gives center frequencies as shown in Table 1. In Table 1, only the upper side band was used for the reference mode-C sequences, so the channel starts at the tabulated frequency and extends 2-MHz above it. For the new sequences, intended to be mode-A (upper and lower side bands), the channel is centered on the tabulated frequency, with a 4-MHz total width. The offsets from the nominal 8200- and 8600-MHz edges of X-band are to avoid edge effects of the video converters. The shift of 3 MHz in the center frequencies as compared with the reference array is due to the need to offset the upper and lower side bands from multiples of 5 MHz to avoid resonant interference from the local clocks. This array was chosen for its low side lobes near the main peak combined with its good resolution characteristics.

Figures 7(c) and 7(d) show the reference array and its ACF, which arise from the sequences:

$$f_{ref} = (8215 + \nu_{ref} \times 5) \text{ MHz} \tag{32}$$

$$\nu_{ref} = (0, 2, 6, 15, 44, 63, 69, 72, 73) \tag{33}$$

which also are expressed in channel frequencies in Table 1.

Figure 8 shows the delay functions for these two array patterns, with the reference delay function in dotted lines, estimated by directly transferring the 2-MHz array sequence to one with 4-MHz mode-A channels. The plots show that, near the central maximum, the reference spectrum has approximately 40 percent higher side lobes than the spectrum generated from the array in Eq. (30).

The measured average PSR of the newly generated spectrum is 7.10 within the region shown, whereas the reference spectrum has a PSR of 5.68, a reduction of approximately 20 percent. This is consistent

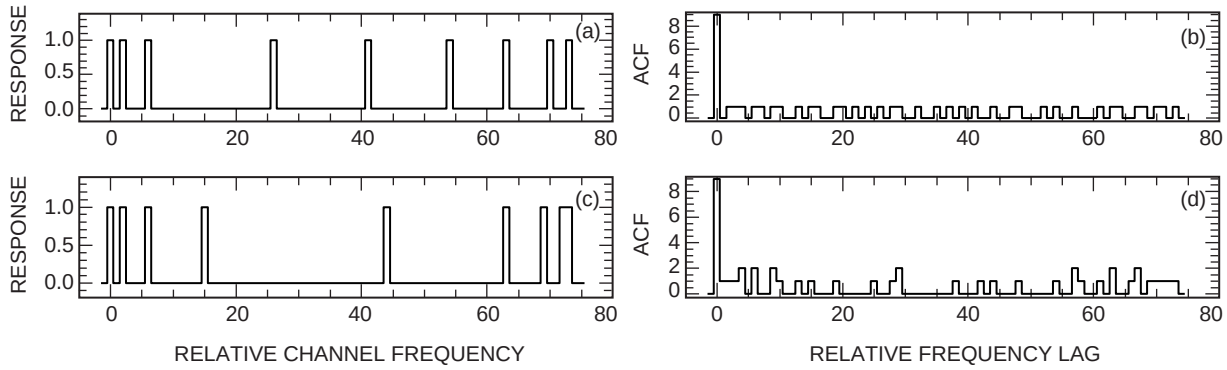

Fig. 7. Two X-band cases: (a) the filter-bank pattern for a near-optimal array generated from Eqs. (30) and (31), (b) the ACF for the same near-optimal pattern, (c) the filter-bank pattern from a reference array used in previous observations and adapted to the mode-A channel size of 4 MHz rather than its original 2 MHz, and (d) the ACF of the reference pattern. The ACFs show that the reference pattern has some redundancy (K = 8), which generates the higher side lobes, but gains higher density near the edges of the band and, thus, slightly higher resolution.

Table 1. Channel frequency values for new mode-A sequences, and reference sequences (mode-C) for comparison, with the center frequency given for each channel.

Channel	Reference X-band, MHz	New X-band, MHz	Reference S-band, MHz	New S-band, MHz
1	8215.76	8212.23	2200.24	2202.24
2	8225.24	8222.24	2206.26	2207.26
3	8245.23	8242.26	2232.74	2232.74
4	8300.24	8342.24	2280.23	2282.23
5	8437.76	8417.24	2297.76	2297.76
6	8530.24	8482.24	—	—
7	8562.24	8527.24	—	—
8	8576.26	8562.26	—	—
9	8580.77	8577.77	—	—

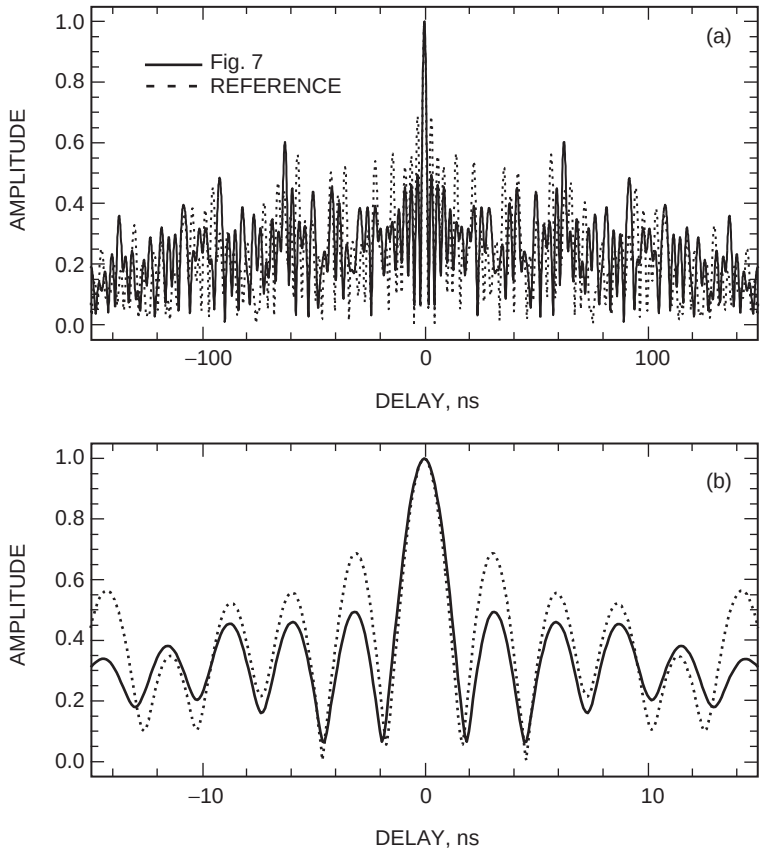

Fig. 8. The DRFs for (a) the X-band patterns shown in Fig. 7 and (b) the region near the central maximum.

with expectations from the previous section, which discussed the PSR (cf., Fig. 3). For the reference array, the redundancy parameter, $K = 8$, and the corresponding expected decrease in average PSR (for the power spectrum) is approximately 18 percent. This suggests a direct correspondence of PSR from power spectral density to the absolute value of the amplitude spectrum, although the effects of the $\sin c$ function also must be considered here.

The slightly higher resolution of the reference spectrum comes from the higher density of channels near the edges of the bandpass; however, this comes at the expense of a higher local level of side lobes near the central maximum. This is expected, since the Fourier transform relationship between the channel frequency and fringe delay regimes here ensures that the largest channel spacings (highest spectral separation) will have the largest effect on the smallest delay regime, that region near the central maximum at zero delay.

B. S-Band (2.2 to 2.3 GHz])

Since, for the typical configurations for VLBI observing, the S-band filter bank uses only 5 to 6 channels, and two of these are fixed at the band edges, this algorithm does not add much additional information. Almost any choice of patterns is nonredundant, and the inner three channels typically must be placed away from the edges to avoid large side-lobe problems. Since S-band observations typically are used only for ionosphere charged-particle calibration, the quality of the S-band BWS array is much less critical to the group delay estimation as compared with X-band (8.2 to 8.6 GHz).

A reference S-band sequence in recent use for geodetic and astrometric VLBI observations and an adapted version that accommodates the larger 4-MHz channel bandwidth for mode-A observations are

included in Table 1. The reference spectrum in this case was already nonredundant, and Fig. 9 shows a comparison between the channel bandpass effects, in contrast to the previous figure, where both spectra were evaluated for mode-A (4-MHz) channels. Thus, the dotted lines show the reference spectrum with 2-MHz channels, and the solid line the adapted spectrum (with frequencies that can be seen in Table 1 to be only slightly changed, primarily to adapt to the larger channels). It is evident that increasing the channel bandwidth results in significant improvement in the peak-to-side-lobe ratio of the DRF, and this applies equally to any type of array that is used. Appendix B also presents some additional analysis of the S-band array characteristics.

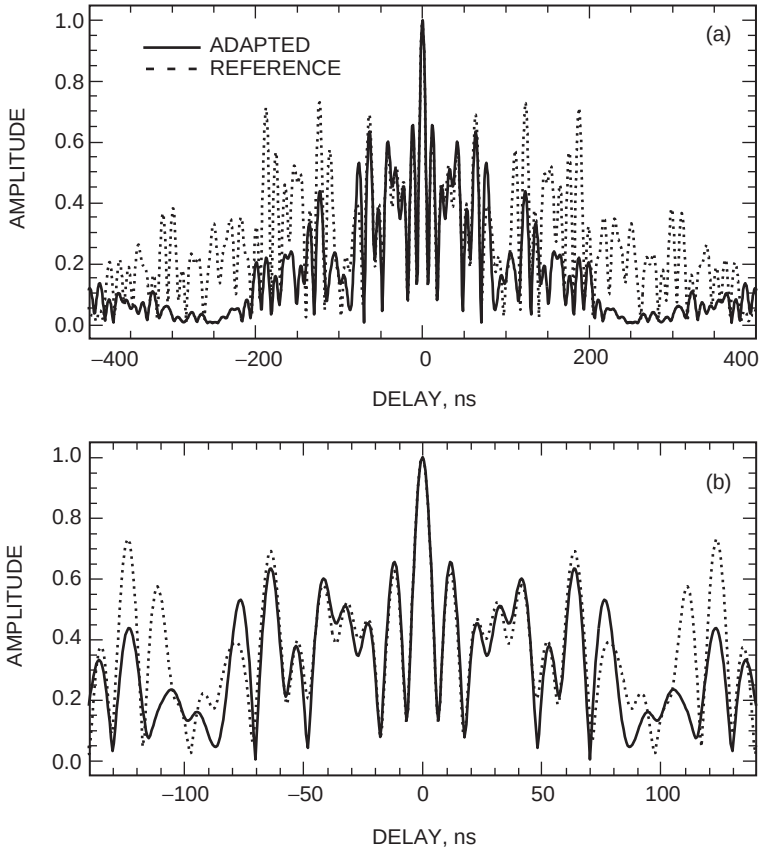

Fig. 9. The DRFs for (a) the S-band arrays in Table 1 and (b) the region near the central maximum. The spectrum was generated using the mode-C individual channel bandwidth of 2 MHz to show the change in the spectrum due to the change in channel bandwidth. The solid line shows the slightly modified five-channel array adapted for mode-A observations. Here it is the sin *c* modulation of the channel bandpass that affects the local PSR rather than the choice of channels since the reference array already is nonredundant.

V. Conclusions

Significant improvement can be made in the choice of filter-bank channels for bandwidth synthesis if the array chosen also has a nonredundant autocorrelation. Combining this with methods to search for those configurations that have the highest possible resolution has yielded some improved filter-bank array patterns that can be used with 4-MHz-wide channels at X-band. The method easily is adapted to other configurations and could be used to design channel arrays for larger channel bandwidths as they become technically feasible.

References

[1] L. D. Baumert, "Cyclic Difference Sets," *Lecture Notes in Mathematics*, no. 182, Berlin: Springer Verlag, 1971.

[2] M. H. Finger and T. A. Prince, *Proc. 19th Intl. Cos. Ray Conf.*, vol. 3, pp. 295–299, 1985.

[3] J. Goodman, *Statistical Optics*, New York: Wiley, 1985.

[4] M. J. E. Golay, *JOSA*, vol. 61, pp. 272–273, 1971.

[5] R. S. Gottesman and E. E. Fenimore, *Applied Optics*, vol. 28, no. 20, pp. 4344–4352, 1989.

[6] L. E. Kopilovich, and L. G. Sodin, *IEE Proc. H: Microwaves, Antenn., Propag.*, vol. 138, no. 3, pp. 233–237, 1991.

[7] A. T. Moffet, *IEEE Trans. AntennṖrop.*, vol. AP-16, no. 2, pp. 172–175, 1968.

[8] A. E. E. Rogers, *Radio Science*, vol. 5, no. 10, pp. 1239–1247, 1970.

Appendix A

Signal-to-Noise Ratios for Nonredundant and Partially Redundant Cases

Equation (23) may be used to construct an estimate of the variance of the square of the DRF, $|\gamma(\tau)|$. The variance is determined from the standard estimator:

$$\begin{aligned}
\sigma^2(|\gamma|^2) &= \langle|\gamma(\tau)|^4\rangle - (\langle|\gamma(\tau)|^2\rangle)^2 \\
&= \frac{\int_0^{\tau_1}|\gamma(\tau)|^4 d\tau}{\int_0^{\tau_1} d\tau} - \left(\frac{\int_0^{\tau_1}|\gamma(\tau)|^2 d\tau}{\int_0^{\tau_1} d\tau}\right)^2 \\
&= \Delta f \int_0^{\tau_1}|\gamma(\tau)|^4 d\tau - \Delta f^2 \left(\int_0^{\tau_1}|\gamma(\tau)|^2 d\tau\right)^2 \qquad \text{(A-1)}
\end{aligned}$$

where $\tau_1 = 1/(\Delta f)$.

Since the amplitude of the central maximum is fixed, the precision of the measurement of the delay from the DRF will depend only on $\sigma^2(|\gamma|^2)$. In this Appendix, we will show that this function is at a minimum for the nonredundant case, and, therefore, the resulting peak-to-side-lobe ratio for the DRF is maximized. Although this will be demonstrated only for the average side-lobe level of the DRF, it suggests that the peak-to-maximum-side-lobe level also will be maximized in general.

For clarity, we have chosen here to estimate the variance of the power spectral density, $|\gamma(\tau)|^2$, rather than the amplitude, $|\gamma(\tau)|$, since the integration over the square-root term again adds complexity without changing the result. (The power spectrum also is positive definite for all τ, whereas the amplitude spectrum must be defined using an absolute value function if negative values are to be avoided; this function is not continuously differentiable.)

To evaluate the integrals in Eq. (A-1), we have restricted the intervals to $0 \leq \tau \leq 1/(\Delta f)$. This interval is of interest since it represents the positive half of the region of the DRF within the first null of the $\sin c$ function due to the individual channel bandpass, and a priori knowledge almost always constrains the true delay to fall within this range of the DRF. Using only the positive limit is acceptable since the DRF is symmetric around $\tau = 0$. For clarity, we also will ignore the effect of the channel bandpass function on the variance $\sigma^2(|\gamma|^2)$. Although the variance is reduced by the $\sin c$ function away from the central maximum (and in fact vanishes at the first null), its modulation is the same for any set of channel spacings, whether redundant or not, and thus adds complexity without changing the result.

Consider the second term on the right-hand side of Eq. (A-1), which is the square of the mean value of the power spectrum $|\gamma(\tau)|^2$:

$$
\begin{aligned}
(\langle|\gamma(\tau)|^2\rangle)^2 &= \Delta f^2 \left[\int_0^{\tau_1} |\gamma(\tau)|^2 d\tau\right]^2 \\
&= \Delta f^2 \left[\int_0^{\tau_1} \left(N + 2\sum_{i=1}^{N-1}\sum_{j>i}^{N} \cos(2\pi(\nu_i - \nu_j)\tau)\right) d\tau\right]^2 \\
&= \Delta f^2 \left[\frac{N}{\Delta f} + 2\sum_{i=1}^{N-1}\sum_{j>i}^{N} \frac{1}{2\pi(\nu_i - \nu_j)} \sin\left(\frac{2\pi(\nu_i - \nu_j)}{\Delta f}\right)\right]^2
\end{aligned}
\tag{A-2}
$$

where we have interchanged the order of integration and summation and evaluated the resulting integral term by term.

Now we assume that

$$\nu_i - \nu_j = m_{ij}\Delta f \tag{A-3}$$

where the m_{ij} are all integers. This means that all channel spacings can be expressed as multiples of the individual channel bandpass. This requirement nominally is always satisfied for $\Delta f << F$, which is true by assumption here, and implies no significant restriction to typical channel array design. Given this, the sine terms in Eq. (A-2) all vanish, since the arguments are multiples of 2π. The result is

$$(\langle|\gamma(\tau)|^2\rangle)^2 = N^2 \tag{A-4}$$

This result is well known, since it also is obtained when one considers the mean of a power spectrum of a Poisson impulsive process of N events, which is analogous to the case of N narrow-frequency channels randomly arranged that we have considered here.

Now consider the mean of the second moment of the power spectrum [the first term in Eq. (A-1)]:

$$\langle|\gamma(\tau)|^4\rangle = \Delta f \int_0^{\tau_1} |\gamma(\tau)|^4 d\tau$$

$$= \Delta f \int_0^{\tau_1} \left[N + 2 \sum_{i=1}^{N-1} \sum_{j>i}^{N} \cos(2\pi(\nu_i - \nu_j)\tau) \right]^2 d\tau$$

$$= N^2 + 4N\Delta f \int_0^{\tau_1} \sum_{i=1}^{N-1} \sum_{j>i}^{N} \cos(2\pi(\nu_i - \nu_j)\tau) d\tau$$

$$+ 4\Delta f \int_0^{\tau_1} \left[\sum_{i=1}^{N-1} \sum_{j>i}^{N} \cos(2\pi(\nu_i - \nu_j)\tau) \right]^2 d\tau$$

$$= N^2 + 4N\Delta f \sum_{i=1}^{N-1} \sum_{j>i}^{N} \frac{1}{2\pi(\nu_i - \nu_j)} \sin\left(\frac{2\pi(\nu_i - \nu_j)}{\Delta f}\right)$$

$$+ 4\Delta f \int_0^{\tau_1} \left[\sum_{i=1}^{N-1} \sum_{j>i}^{N} \cos(2\pi(\nu_i - \nu_j)\tau) \right]^2 d\tau \qquad \text{(A-5)}$$

If we now make the same assumption as above, that all channel spacings are integer multiples of the channel width, the double sum involving only sine terms [the second of three terms in Eq. (A-5)] again vanishes, and only the integral over the square of the sum of cosine terms (the third term) remains to be evaluated. To do this, first convert the double sum to a single sum over $M = N(N-1)/2$ terms, cf., Eq. (20), each of which represents a single possible channel spacing, eg.,

$$\Delta\nu_p = \nu_i - \nu_j, \quad p = 1, 2, \cdots, M \qquad \text{(A-6)}$$

Then we can rewrite the integrand of the third term in Eq. (A-5) as

$$\left(\sum_{p=1}^{M} \cos(2\pi\Delta\nu_p\tau) \right)^2 = \sum_{p=1}^{M} \cos^2(2\pi\Delta\nu_p\tau)$$

$$+ \sum_{p=1}^{M-1} \sum_{q>p}^{M} 2\cos(2\pi\Delta\nu_p\tau)\cos(2\pi\Delta\nu_q\tau) \qquad \text{(A-7)}$$

for which there are M terms involving $\cos^2$ and $M(M-1)/2$ terms involving the cross-product of the cosines of differing arguments.

Evaluating this term by term [and multiplying through the scale factor $4\Delta f$ in Eq. (A-5)], we have

$$4\Delta f \sum_{p=1}^{M} \int_0^{\tau_1} \cos^2(2\pi\Delta\nu_p\tau)d\tau = 4\Delta f \sum_{p=1}^{M} \left[\frac{1}{2\Delta f} + \frac{1}{8\pi\nu_p}\sin\left(\frac{4\pi\nu_p}{\Delta f}\right)\right]$$

$$= 2M + \sum_{p=1}^{M}\left[\frac{\Delta f}{2\pi\nu_p}\sin\left(\frac{4\pi\nu_p}{\Delta f}\right)\right] \tag{A-8}$$

The second set of terms in Eq. (A-7), involving the double sums over cross-products of cosine terms, can be evaluated in similar fashion (again including the scale factor):

$$4\Delta f \sum_{p=1}^{M-1}\sum_{q>p}^{M} \int_0^{\tau_1} 2\cos(2\pi\Delta\nu_p\tau)\cos(2\pi\Delta\nu_q\tau)d\tau =$$

$$4\Delta f \sum_{p=1}^{M-1}\sum_{q>p}^{M}\left[\frac{\sin\left(\frac{2\pi(\Delta\nu_p-\Delta\nu_q)}{\Delta f}\right)}{(\Delta\nu_p-\Delta\nu_q)} + \frac{\sin\left(\frac{2\pi(\Delta\nu_p+\Delta\nu_q)}{\Delta f}\right)}{(\Delta\nu_p+\Delta\nu_q)}\right],\ \Delta\nu_p^2 \neq \Delta\nu_q^2 \tag{A-9}$$

where the restriction is imposed to avoid the singularity in the first sine term in the double sum. In fact, the restriction is not necessary for a purely nonredundant set of channel spacings, since by assumption it is satisfied.

However, suppose there are K such redundant pairs of channel spacings such that $\Delta\nu_r^2 = \Delta\nu_s^2$ for some set $\{r, s\}$. For each of these K terms, the integrand can be rewritten:

$$2\cos(2\pi\Delta\nu_r\tau)\cos(2\pi\Delta\nu_s\tau) = 2\cos^2(2\pi\Delta\nu_r\tau) \tag{A-10}$$

which thus reduces the double sum to only a single sum over r of these K terms. Thus, Eq. (A-9) becomes

$$4\Delta f \sum_{p=1}^{M-1}\sum_{q>p}^{M} \int_0^{\tau_1} 2\cos(2\pi\Delta\nu_p\tau)\cos(2\pi\Delta\nu_q\tau)d\tau = 4K + \sum_{p=1}^{K}\left[\frac{\Delta f}{2\pi\nu_p}\sin\left(\frac{4\pi\nu_p}{\Delta f}\right)\right] +$$

$$4\Delta f \sum_{p=1}^{M-1}\sum_{q>p}^{M}\left[\frac{\sin\left(\frac{2\pi(\Delta\nu_p-\Delta\nu_q)}{\Delta f}\right)}{(\Delta\nu_p-\Delta\nu_q)} + \frac{\sin\left(\frac{2\pi(\Delta\nu_p+\Delta\nu_q)}{\Delta f}\right)}{(\Delta\nu_p+\Delta\nu_q)}\right],\ \Delta\nu_p^2 \neq \Delta\nu_q^2 \tag{A-11}$$

Once again we apply the requirement that the channel spacings be integral multiples of the channel width, eg, $\Delta\nu_p = m_p\Delta f$. Then, as before, all of the sine terms in these equations vanish. What remains can be collected from Eqs. (29), (30), (33), and (36) to yield

$$\sigma^2(|\gamma|^2)(K) = N^2 + 2M + 4K - N^2$$

$$= N^2 + N(N-1) + 4K - N^2$$

$$= N^2 - N + 4K \tag{A-12}$$

where the factor K expresses the level of redundancy as the number of pairs of channels that have equal spacings (to within the resolution of Δf). The peak-to-rms-side-lobe ratio (PSR) for the power spectrum then can be expressed as

$$PSR(N,K) = \frac{|\gamma(0)|^2 - \langle|\gamma(\tau)|^2\rangle}{\sqrt{N^2 - N + 4K}}$$

$$= \frac{N^2 - N}{\sqrt{N^2 - N + 4K}} \tag{A-13}$$

For the nonredundant case ($K = 0$), this reduces to

$$PSR(N,0) = \sqrt{N^2 - N} \tag{A-14}$$

Appendix B
Delay Resolution Functions of BWS Arrays Used in Recent VLBI Observations

This appendix documents a number of S-/X-band BWS arrays used in recent geodetic VLBI observations. These arrays were used in mode-C observations, when the individual channel bandpass is the 2-MHz upper side band relative to the center frequency. In Table B-1, the channel frequency values (lower end of the 2-MHz channel) are noted for the sequence commonly used for geodetic observations at JPL and GSFC. Note that JPL commonly uses a 5/9 S-/X-band configuration, whereas GSFC uses a 6/8 configuration.

Table B-1. Bandwidth synthesis arrays used in recent mode-C VLBI observations by JPL or GSFC.

Channel	JPL X-band, MHz	GSFC X-band, MHz	JPL S-band, MHz	GSFC S-band, MHz
1	8215.76	8210.49	2200.24	2217.49
2	8225.24	8220.49	2206.26	2222.49
3	8245.23	8250.49	2232.74	2237.49
4	8300.24	8310.49	2280.23	2267.49
5	8437.76	8420.49	2297.76	2292.49
6	8530.24	8500.49	—	2302.49
7	8562.24	8550.49	—	—
8	8576.26	8570.49	—	—
9	8580.77	—	—	—

I. Sequence Design Philosophy

The philosophy of the sequences also is somewhat different: the JPL sequences have been designed toward achieving the highest possible resolution, with only moderate concern for main-lobe SNR, since the ambiguities almost always are resolvable, even if the side-lobe level is approximately 60 percent or so. Because X-band provides a larger bandpass and usually better SNR in geodetic observations than does S-band, the channel division is weighted toward X-band (nine channels versus five).

The GSFC philosophy has emphasized a sequence with more even spacings, which produces a very high side lobe (approximately 90 percent or more) at a position with a fixed delay, ±100 ns. This delay ambiguity is resolved easily by external considerations for normal data sets. The central lobe delay resolution is not emphasized as much. The channel division also is more even (8/6), which provides a greater level of immunity to channel dropouts at S-band, but less strength in the X-band delay resolution.

II. Delay Resolution Functions for the Sequences

A. S-Band

Figure B-1 shows the S-band DRF for the standard JPL sequence, which uses only five channels. The maximum side lobe is at about 65 percent of the main lobe. In Fig. B-2, the DRF is shown for the case when one channel has dropped out, leading to a maximum side lobe that is much higher (80 percent) and very near the main lobe. It is evident that channel dropouts from the JPL S-band sequence easily could lead to misidentified solutions in S-band.

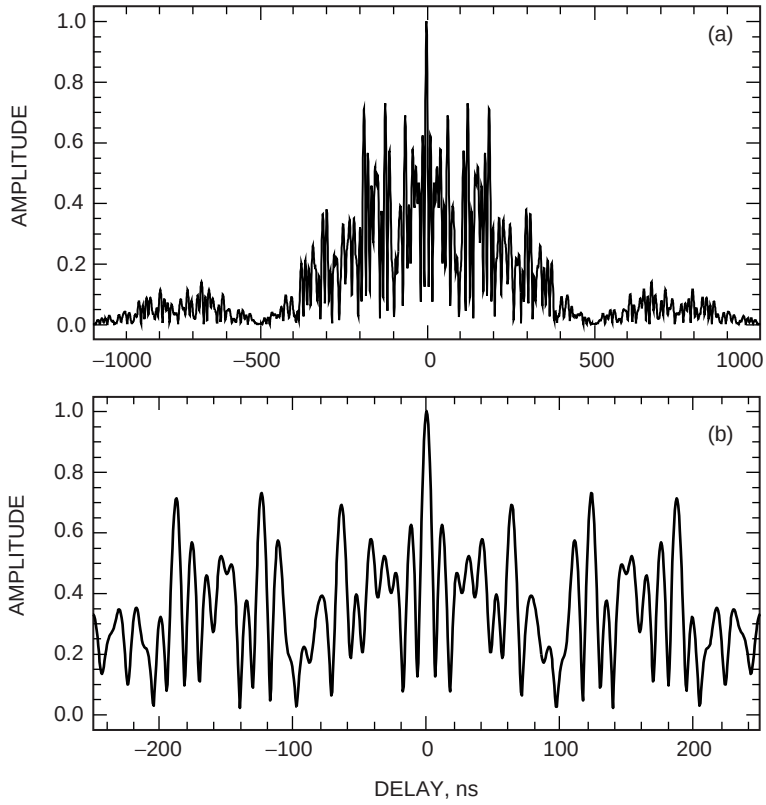

Fig. B-1. The DRF for (a) the S-band JPL nominal mode-C sequence and (b) the region near the central maximum.

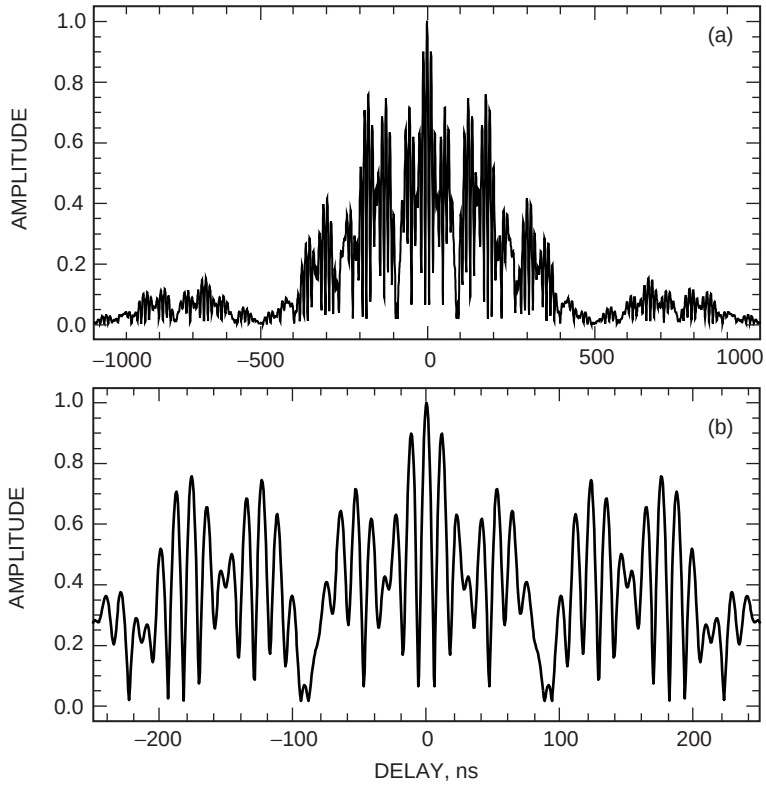

Fig. B-2. The DRF for (a) the S-band nominal JPL sequence with one of the central channels missing in order to look at the degradation of the DRF and (b) the region near the central maximum.

Figures B-3 and B-4 show the same pair of plots for the GSFC sequence: first the nominal sequence DRF, and then the DRF with one of the central channels missing. It is evident that the GSFC S-band sequence has superior SNR as compared with the JPL sequence, but this is due in part to the fact that six channels are used instead of five. The loss of a channel is also much less of a problem for the GSFC sequence at S-band.

Figure B-5 shows a comparison of the time resolution of the JPL and GSFC delay resolution functions. The JPL DRF has approximately 20 percent better resolution (at 90 percent of the maximum), in spite of the fact that one less channel is used. This is due mainly to the fact that the JPL sequence tends to put the channels near the band edges, while the GSFC sequence uses a more even channel spacing.

B. X-Band

Figures B-6 through B-10 show the same series of plots for the X-band sequences. Again, in each case the DRF of the sequence is shown both for the nominal sequence and for the case of one of the central channels missing. Here the GSFC sequence again is seen to have a higher immunity to channel dropouts (at least near the central channels) than does the JPL sequence, even though it utilizes one less channel to begin with.

The series of DRF plots concludes with a comparison of the time resolution, where the JPL sequence shows approximately 10 percent better resolution (at 90 percent of the maximum) for the same reason as in the S-band case: more emphasis on placing channels near the band edges. Thus, in summary, the two sequences show distinct advantages or disadvantages depending upon the data quality. For data that are robust with respect to channel dropouts, and of high SNR, the JPL sequence probably is better in all respects, but for data with dropout problems, the JPL sequence runs a risk of higher levels of ambiguity, and the GSFC sequences are more robust at the expense of delay resolution in the central lobe.

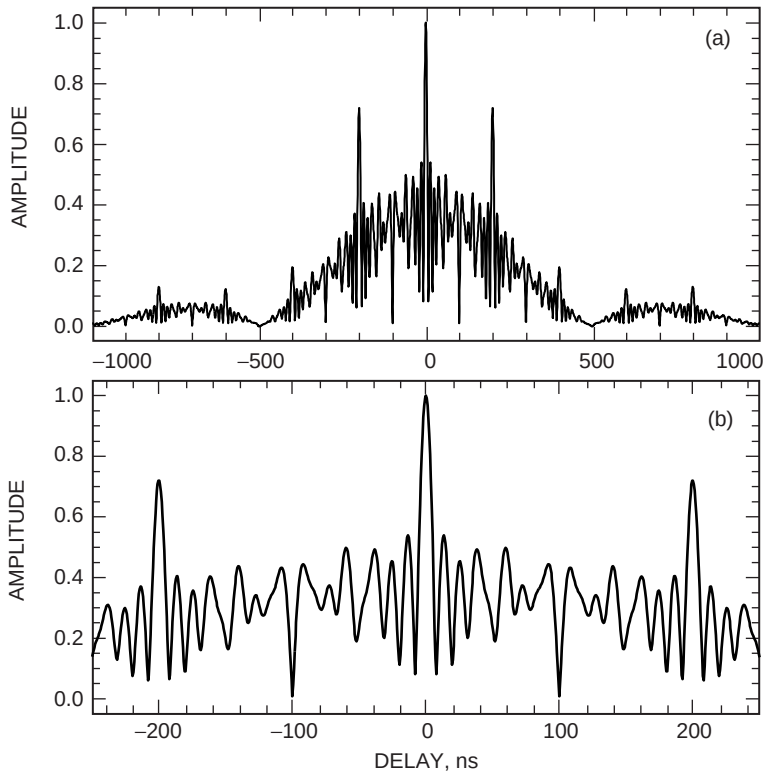

Fig. B-3. The DRF for (a) the S-band nominal GSFC sequence and (b) the region near the central maximum. (Similar to Fig. B-1.)

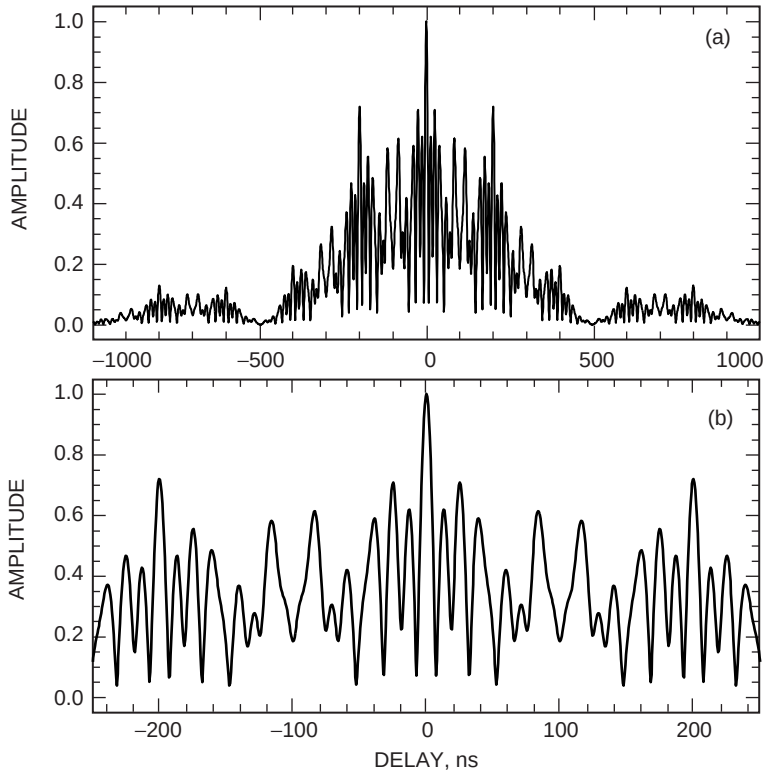

Fig. B-4. The DRF for (a) the S-band nominal GSFC sequence with one of the central channels missing and (b) the region near the central maximum. (Similar to Fig. B-2.)

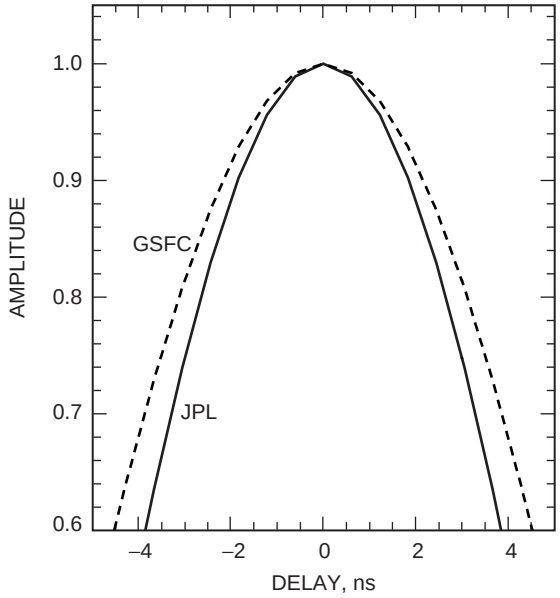

Fig. B-5. Comparison of time resolution for the JPL and GSFC nominal sequences for mode-C operation at S-band.

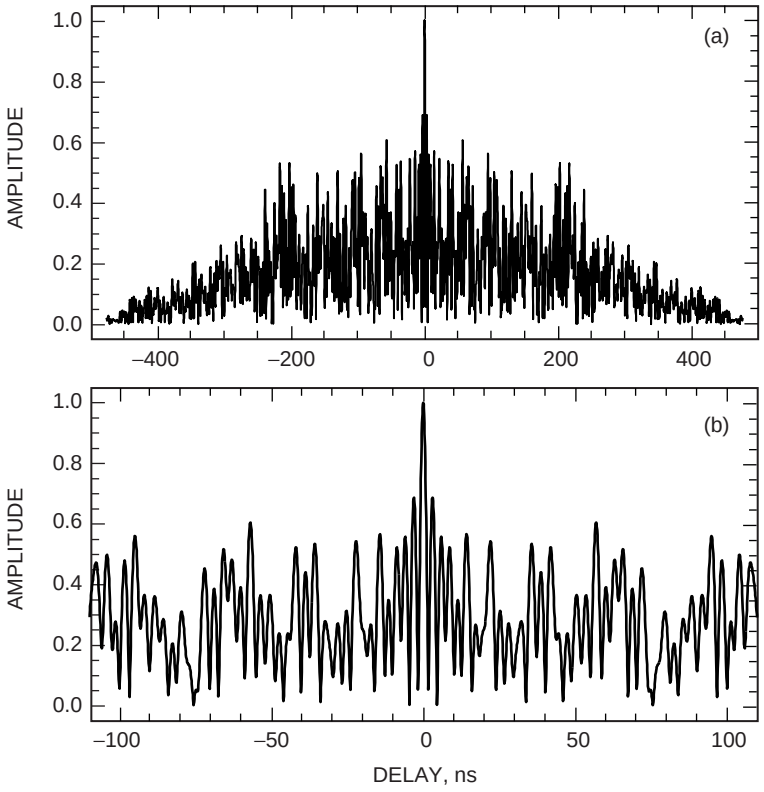

Fig. B-6. The DRF for (a) the X-band JPL nominal mode-C sequence and (b) the region near the central maximum. (Similar to Fig. B-1.)

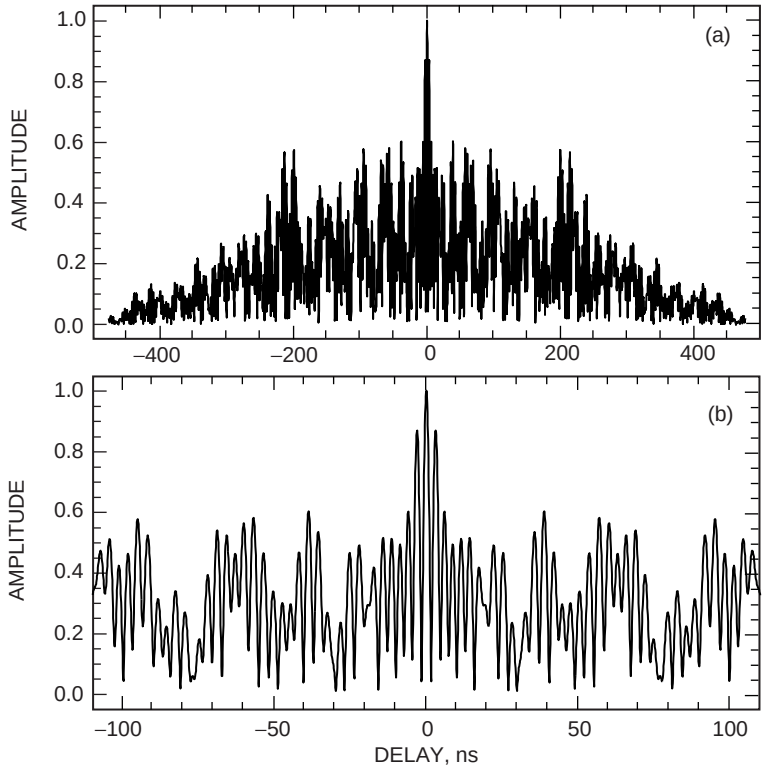

Fig. B-7. The DRF for (a) the X-band nominal JPL sequence with one of the central channels missing and (b) the region near the central maximum. (Similar to Fig. B-2.)

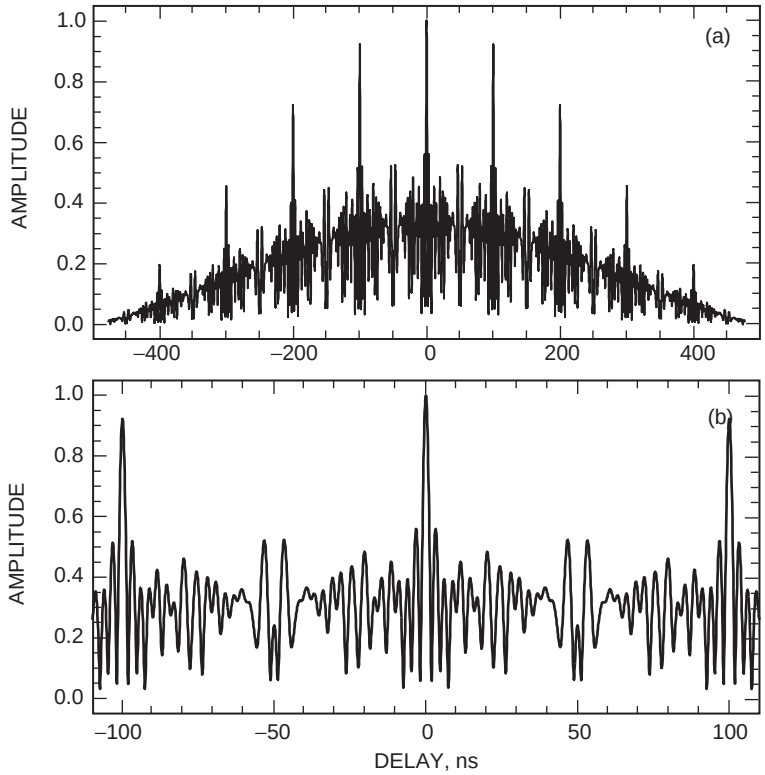

Fig. B-8. The DRF for (a) the X-band nominal GSFC sequence and (b) the region near the central maximum. (Similar to Fig. B-3.)

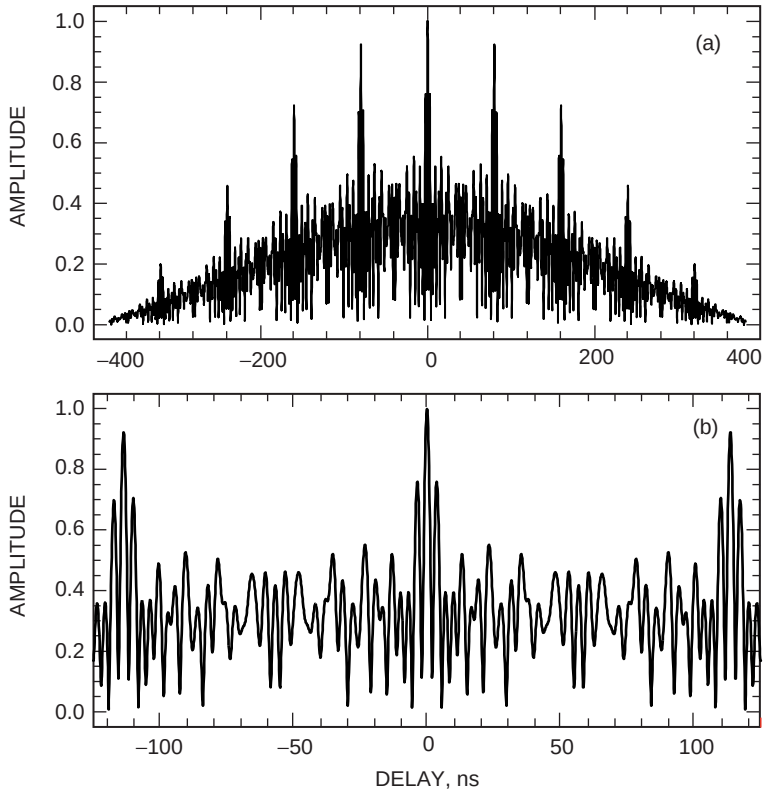

Fig. B-9. The DRF for (a) the X-band nominal GSFC sequence with one of the central channels missing and (b) the region near the central maximum. (Similar to Fig. B-4.)

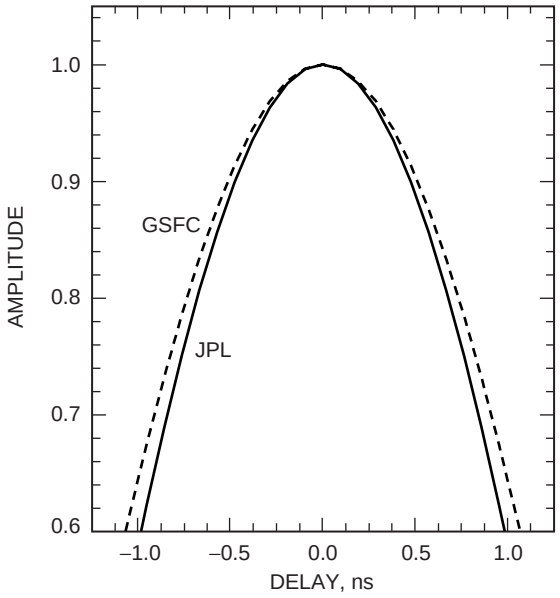

Fig. B-10. Comparison of time resolution for the JPL and GSFC nominal sequences for mode-C operation at X-band.